Received: 8 May 2020 | Revised: 9 July 2020 | Accepted: 11 July 2020

DOI: 10.1002/aic.16988

AIChE JOURNAL

TRIBUTE TO FOUNDERS: KEITH GUBBINS. THERMODYNAMICS AND MOLECULAR-SCALE PHENOMENA

Predicting chemical reaction equilibria in molten carbonate fuel cells via molecular simulations

Jeffrey M. Young[1] | Anirban Mondal[1] | Timothy A. Barckholtz[2] | Gabor Kiss[2] | Lucas Koziol[2] | Athanassios Z. Panagiotopoulos[1]

[1]Department of Chemical and Biological Engineering, Princeton University, Princeton, New Jersey

[2]ExxonMobil Research and Engineering, Annandale, New Jersey

Correspondence
Athanassios Z. Panagiotopoulos, Department of Chemical and Biological Engineering, Princeton University, Princeton, NJ.
Email: azp@princeton.edu
Lucas Koziol, ExxonMobil Research and Engineering, Annandale, NJ.
Email: lucas.koziol@exxonmobil.com

Funding information
Basic Energy Sciences, Grant/Award Number: DE-SC0002128; ExxonMobil Research and Engineering Company, Grant/Award Number: EM09125.A1

Abstract

It has been recently suggested that hydroxide ions can be formed in the electrolyte of molten carbonate fuel cells when water vapor is present. The hydroxide can replace carbonate in transporting electrons across the electrolyte, thereby reducing the CO_2 separation efficiency of the fuel cell although still producing electricity. In this work, we obtain the equilibrium concentration of hydroxide in five molten alkali carbonate salts from molecular simulations. The results reveal that there can be a substantial amount of hydroxide in the electrolyte at low partial pressures of CO_2. In addition, we find that the equilibrium concentration of molecular water dissolved in the electrolyte is over two orders of magnitude higher than that of CO_2. Increasing the size and polarizability (or in other words reducing the "hardness") of the cations present in the electrolyte can reduce the hydroxide fraction, but at the cost of lowering ionic conductivity.

KEYWORDS

molecular simulation, molten carbonate fuel cell, reaction equilibrium

1 | INTRODUCTION

In an era of rising energy demand associated with the need to reduce greenhouse gas emissions, molten carbonate fuel cells (MCFCs) have emerged as a potential solution for removing CO_2 from flue gases.[1-3] In addition to extracting CO_2, MCFCs are able to generate electricity at high fuel-to-energy conversion efficiency.[4,5] The value of the electricity generated in this process offsets the costs of carbon capture, potentially making MCFCs one of the most promising technologies for the generation of clean energy from fossil fuels. MCFCs can also produce low greenhouse gas hydrogen as a co-product, further enhancing the value proposition.[6,7]

An MCFC consists of a porous lithiated NiO cathode, a matrix separator containing the bulk of the electrolyte, and an anode made from a Ni based alloy.[8-10] MCFC electrolytes are typically based on eutectic mixtures of Li/Na and Li/K carbonates. These eutectic mixtures have melting points 200–300°C below that of the pure carbonates, allowing MCFCs to operate at lower temperatures around 600°C. In MCFC operation, CO_2 and O_2 from the flue gas are passed over the porous cathode, where they dissolve into the electrolyte. Upon oxygen reduction, the two species combine to form carbonate ions (Equation 1). This carbonate is then transported through the matrix to the anode, where it is reduced in the presence of hydrogen (Equation 2). The exact mechanism of this reaction has been discussed in the literature, and is not the subject of the current work.[11,12]

$$\text{Cathode}: \ CO_2 + \frac{1}{2}O_2 + 2e^- \rightarrow CO_3^{2-} \tag{1}$$

$$\text{Anode}: \ H_2 + CO_3^{2-} \rightarrow H_2O + CO_2 + 2e^- \tag{2}$$

However, recent experiments have revealed a parallel oxygen reduction mechanism when operating at low CO_2 gas-phase

Jeffrey M. Young and Anirban Mondal contributed equally to this work.

concentration and high current density.[13] Measurements suggest a net consumption of water at the cathode, caused by water reacting with oxygen to produce hydroxide ions.

$$\frac{1}{2}O_2 + H_2O + 2e^- \rightarrow 2OH^- \quad (3)$$

In this alternate electrochemical process, it is the hydroxide ions that are transported from cathode to anode instead of carbonate. While this process still contributes to power generation, it does not contribute to CO_2 capture from the cathode feed and thus reduces the carbon capture efficiency of the cell. Previous studies have emphasized the role of hydroxide ions as an intermediate reactant and as the principal water-derived species in molten carbonates.[14,15] Hydroxide ions have also been implicated in cell degradation through the evaporation of alkali hydroxide species.[16] Although the cathode reactions may be kinetically limited, understanding the carbonate-hydroxide reaction equilibrium in molten carbonates is an appropriate first step towards understanding the overall process.

Experimentally, investigating the key interactions governing the carbonate-hydroxide equilibrium is challenging because MCFCs operate at high temperatures, approximately 600–650°C, and spectroscopic measurements at those conditions are difficult.[17] In light of this challenge, computational approaches are an attractive alternative. A number of methods have been proposed for the calculation of chemical reaction equilibria using molecular simulations. These include reaction ensemble Monte Carlo,[18] reactive force fields,[19] and reaction ensemble molecular dynamics (ReMD).[20] The reaction ensemble Monte Carlo method adds a move to Monte Carlo simulations that exchanges the reactant and product species of a reaction. However, this move is difficult in dense systems, especially if the reacting species are large.[18] Reactive force fields are classical force fields that allow formation and dissociation of chemical bonds. These simulations can give reaction rates as well as equilibrium compositions, assuming that the accessible simulation timescales match the kinetics of the system in question. However, reactive force fields are challenging to parameterize.[21] An alternative method is the recent ReMD implementation by Smith and Qi which permits the calculation of chemical reaction equilibria in dense systems using atomistic molecular models.[20] In this method, the chemical potentials of the reacting species are calculated at a guess for the equilibrium composition, and then an ideal solution approximation is used to estimate the true equilibrium concentration. This process is repeated until the composition converges. The key advantage of Smith and Qi's ReMD method is that chemical potentials of large molecules and ions can be computed from molecular dynamics, even in dense fluid phases. We therefore utilized a similar ReMD method in this work, as described in the method section.

This work is divided into four parts. The introduction is followed by the details of the force fields used to model carbonate, hydroxide, CO_2, and H_2O. Then we describe the simulation methods employed to calculate the chemical reaction equilibria, standard state free energy of formation, and chemical potentials. In the subsequent section, we calculate the dependence of the carbonate-hydroxide chemical reaction equilibrium on CO_2 partial pressure and cation composition, and we determine the concentration of dissolved molecular H_2O and CO_2 in the electrolyte. The last section summarizes our findings and provides the implications for MCFCs.

1.1 | Models

A handful of force fields exist for modeling molten alkali metal carbonates and hydroxides.[22-27] However, most of these models have shortcomings when trying to simultaneously describe physical properties (e.g., density, diffusivity, conductivity, viscosity, etc.) and chemical potentials. In an accompanying work, we have parameterized new force fields for alkali carbonate and hydroxide electrolytes that accurately reproduce both thermodynamic and transport properties.[28] Specifically, these models predict the experimental chemical potentials of the pure carbonate and hydroxide salts to within $\sim 1kT$.

To enable accurate chemical potential calculations, all ions in our model possess full charges. The model assumes a rigid hydroxide bond and a fully flexible carbonate molecule including harmonic bond and angle terms and a 4-center torsion. The intermolecular cation–cation interaction is represented by Coulomb repulsion, while cation-anion and anion-anion interactions are represented by a combination of Buckingham and Coulomb terms. Mason-Rice combining rules, which are analogous to the Lorentz-Berthelot rules for the Lennard-Jones potential, are used for the hydroxide-carbonate cross-interactions (arithmetic mean for the size and geometric mean for the energy parameters).[29,30] The functional forms of the interactions and combining rules are given in Equations (1)–(4) of the Supporting Information (SI).

We model CO_2 and H_2O interactions with the electrolyte using literature force fields and Mason-Rice combining rules. Both species are described by point-charge plus Buckingham interactions. Specifically, the interaction parameters for CO_2 are taken from Tsuzuki et al[31] and Cygan et al[32] A recently parameterized TIP3P style Buckingham potential is adopted to model H_2O.[33] While the C—O covalent bonds in the CO_2 molecule are treated as flexible bonds, the O—H bonds and angles in the H_2O molecule are assumed to be rigid. Mason-Rice combining rules lend the Buckingham cross interaction parameters between CO_2, H_2O, and the cations by using an effective cation–cation interaction computed from reversing the combining rules on the cation-carbonate parameters. Because the CO_2 and H_2O force fields are not parameterized for these conditions, we do not expect the results to be quantitatively true. Having said that, we must also mention that the performance of the pure H_2O and CO_2 potentials at high temperatures is not the best measure of the performance of the potentials in the molten carbonate and hydroxide. The simulations performed in this work involve only a single H_2O or CO_2 molecule in a system of large number of ions, so the important parameters are the cross interactions between the inserted molecule and the carbonate, hydroxide, and the alkali cations. Therefore, we expect that these models will still provide at least rough estimates of the dissolved gas concentrations. All bonded and non-bonded force field parameters utilized in this study are tabulated in Tables S1–S3.

2 | METHODS

2.1 | Chemical reaction equilibrium calculations

The goal of this work is to determine the equilibrium concentrations of hydroxide and carbonate ions in MCFC electrolytes as a function of the partial pressure of CO_2 and H_2O. Subtracting Equations (1) and (3) yields the carbonate hydrolysis equilibrium which gives a relation between the concentrations of CO_3^{2-} and OH^- in the melt.

$$CO_3^{2-}(l) + H_2O(g) \leftrightarrow 2OH^-(l) + CO_2(g) \tag{4}$$

A chemical reaction is at equilibrium when the sum of the chemical potentials of the products is equal to that of the reactants, or for the case of carbonate hydrolysis,

$$\mu_{CO_3^{2-},l} + \mu_{H_2O,g} = 2\mu_{OH^-,l} + \mu_{CO_2,g} \tag{5}$$

where μ is the chemical potential of each species. To compute this chemical potential, we can break it up into three components:

$$\mu = \Delta_f G^0 + \mu^{IG} + \mu^{EX} \tag{6}$$

where $\Delta_f G^0$ is the standard formation free energy of the ideal gas species, μ^{IG} is the ideal gas part of the chemical potential, and μ^{EX} is the excess chemical potential. While the $\Delta_f G^0$ values for most neutral molecules and monovalent ions can be readily found in the literature, they are not available for divalent ions, such as carbonate.[34] Therefore, the value for the CO_3^{2-} ion must be determined by other means, such as quantum chemical calculations.

The ideal gas chemical potential is given by

$$\mu^{IG} = RT\ln\left(\frac{NkT}{P_0\langle V\rangle}\right) \tag{7}$$

where $\langle V\rangle$ is the simulation volume, R is the ideal-gas constant, T is the absolute temperature, N is the number of molecules in the simulation cell, k is the Boltzmann constant, and P_0 is the reference pressure at which $\Delta_f G^0$ is determined. The excess chemical potential can be calculated for a given force field from classical molecular dynamics simulations, as explained in the following section.

To calculate the reaction equilibrium in Equation (5), we make two simplifying assumptions: (1) only alkali hydroxide and carbonate are present in the electrolyte, and (2) the vapor phase follows the ideal gas law. The first assumption means that the dissolved concentrations of typical cathode feed components, such as CO_2, H_2O, O_2, and N_2 are negligible and that other potential reactions, such as formation of pyrocarbonate[35-37] or reduced oxygen species,[38,39] do not introduce significant concentrations of additional species.

Because we assume that the gas phase is an ideal gas, we can set the excess chemical potential equal to zero for the gaseous CO_2 and H_2O. This leaves us with

$$\mu_{H_2O} = \Delta_f G^0_{H_2O} + RT\ln\left(\frac{P_{H_2O}}{P_0}\right) \tag{8}$$

and

$$\mu_{CO_2} = \Delta_f G^0_{CO_2} + RT\ln\left(\frac{P_{CO_2}}{P_0}\right) \tag{9}$$

where P_{H_2O} and P_{CO_2} are the partial pressures of water and CO_2 in the gas, respectively. Typically the partial pressure of water is nearly constant in the fuel cell, but the partial pressures of O_2 and CO_2 decrease from the inlet to outlet as they are removed from the gas phase. Therefore, we can solve Equations (5), (8), and (9) for P_{CO_2}.

$$P_{CO_2} = P_0\exp\left[\left(\Delta_f G^0_{H_2O} + RT\ln\left(\frac{P_{H_2O}}{P_0}\right) + \mu_{CO_3^{2-}} - 2\mu_{OH^-} - \Delta_f G^0_{CO_2}\right)\left(\frac{1}{RT}\right)\right] \tag{10}$$

At a given P_{H_2O}, the only unknowns in Equation (10) are $\mu_{CO_3^{2-}}$ and μ_{OH^-} as a function of the concentrations of carbonate and hydroxide in the melt. To calculate these chemical potentials, the formation free energy and μ^{EX} must be determined for both species. Since these chemical potentials are dependent upon the alkali composition, this process must be repeated for each cation composition.

2.2 | Formation free energy computation

The computation of enthalpies and free energies of formation using ab initio methods has been addressed in the literature using the method summarized here.[40-43] The enthalpy of formation at a given temperature (T) for a chemical species (X) can be expressed as the difference between the enthalpy of the molecule and the enthalpy of the reference state for each atom in the molecule.

$$\Delta_f H^0_X(T) = H_X(T) - \sum_{i=1}^{n} H_{ref,i}(T) \tag{11}$$

One can obtain a more practical expression by expanding Equation (11) as

$$\Delta_f H^0_X(T) = H^{inc}_X(T-0) + E_{0,X} + E_{ZPE,X} - \sum_{i=1}^{n} E_{0,atm,i} + \sum_{i=1}^{n} \Delta_f H^0_i(0) - \sum_{i=1}^{n} H^{inc}_{ref,i}(T-0) \tag{12}$$

where $H^{inc}_X(T-0)$ is the enthalpy increment for the molecule from 0 K to a temperature T, $E_{0,X}$ is the molecular energy at 0 K, $E_{ZPE,X}$ is the zero-point vibrational energy, $E_{0,atm,i}$ is the energy of atom i at 0 K, $\Delta_f H^0_i(0)$ is the ideal gas formation enthalpy of atom i at 0 K, and $H^{inc}_{ref,i}(T-0)$ is the enthalpy increment for the atom i from 0 K to a temperature T. Values for the atomic energies are obtained in their most stable state, for example, the triplet state for an isolated oxygen atom.

Values for $\Delta_f H_i^0(0)$ and $H_{ref,i}^{inc}(T-0)$ are taken from the NIST-JANAF thermochemical tables[34] and all other quantities in Equation (12) are determined from ab initio simulations. Note that if the chemical component under consideration is an ion, one should take into account (add/subtract for cation/anion) the reference state enthalpy increment of an electron gas.

The free energy of formation at a given temperature (T) for a chemical species (X) is then computed as in Equation (13).

$$\Delta_f G_X^0(T) = \Delta_f H_X^0(T) - T\left(S_X - \sum_{i=1}^{n} S_{ref,i}\right) \tag{13}$$

Here, we can directly adopt the absolute entropy values ($S_{ref,\ i}$) from the NIST-JANAF thermochemical tables[34] because they use the same reference state for entropy as the ab initio calculations. The entropy of a molecule (S_X) is computed by the following equation:

$$S_X = \frac{H_X - G_X}{T} \tag{14}$$

where H_X and G_X are the enthalpy and free energy of the molecule at temperature T obtained from quantum chemical calculations. Once again, in the case of an ion, the reference state entropy of an electron gas must be incorporated (added/subtracted for cation/anion) into the entropy difference in Equation (13).

Here, we have employed a series of quantum chemical methods to compute enthalpy and free energy of formation, including density functional theory (DFT), coupled-cluster theory (CCSD), Møller-Plesset (MP2) perturbation theory, and a number of Gaussian compound theories. All gas-phase quantum chemical calculations are performed using the Gaussian16 program.[44] A comparison of performance against experimental measurements for all these methods is provided in Figure 1.

As evident from Figure 1, formation free energies computed using the B3LYP and MP2 methods show large deviations from experiment. We observe that the predictions at the CCSD(T)/aug-cc-pVQZ level are also deficient, exhibiting large differences (with errors up to ~40 kJ/mol) compared to experimental values. The poor performance of coupled-cluster theory compared to a method such as B3LYP does not guarantee that CCSD(T) is a bad choice overall in computing formation free energies when compared to B3LYP. This is true for just a couple of systems (H_2O and OH^-) studied here. In order to obtain a quantitative comparison of the accuracy of these methods, one has to study a large set of molecules/ions and then compare their average deviation from the experiment, as discussed by Allison et al.[43] On the other hand, calculations performed at the CBS-QB3 level provide a better estimation of formation free energy with a maximum deviation from experiment less than 10 kJ/mol. Many recent literature reports have shown that Gaussian compound theories (Gaussian-x) perform exceptionally well in predicting enthalpies of formation for aromatic hydrocarbon compounds and a number of related functionalized molecules.[41,43] Thus, we have also tested the predictions of different Gaussian compound methods. As evident from Figure 1, the

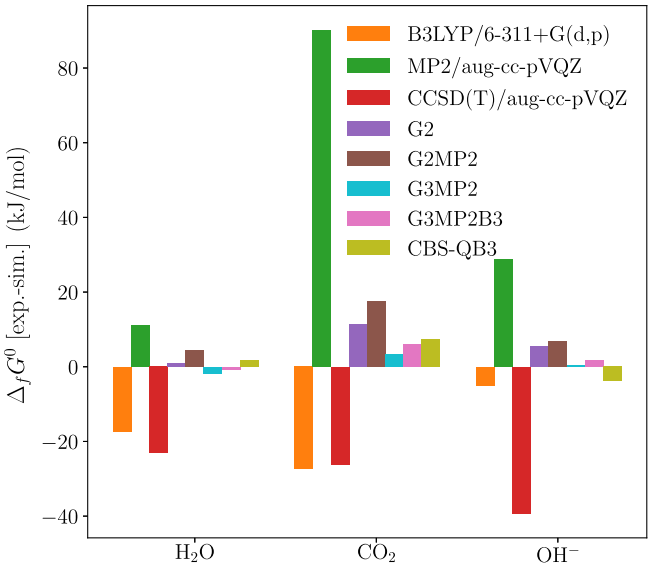

FIGURE 1 Difference in free energy of formation between experiment and quantum chemical calculations performed at different levels of theory. The comparison is done at 298 K and 1 bar [Color figure can be viewed at wileyonlinelibrary.com]

performance of these compound theories is superior to methods like B3LYP, MP2, CCSD(T), and at times CBS-QB3. A possible justification for these observations could be the fact that the Gaussian-x model chemistries include a series of empirical correction terms to obtain molecular energies to high accuracy. The interested reader is directed to the work of Curtiss et al for additional details.[45] Among the different Gaussian-x methods tested, G3MP2 displays the lowest error between the calculated and experimental data, and is used for all quantum chemical calculations in this work. The formation free energy of CO_3^{2-} obtained at the G3MP2 level is −130.12 kJ/mol at 923.15 K. All the thermochemical values for the different species investigated here are provided in Table S4.

2.3 | Excess chemical potential calculation

To calculate the excess chemical potential, we split it into two parts:

$$\mu^{EX} = \mu_{vdW}^{EX} + \mu_{Coul}^{EX} \tag{15}$$

where μ_{Coul}^{EX} is the excess chemical potential due to the Coulomb interactions, and μ_{vdW}^{EX} is the excess chemical potential from the Buckingham part of the potential. The excess chemical potentials for the carbonate and hydroxide ions are calculated from the free energy change of an ion insertion. This free energy change is determined using Bennett's Acceptance Ratio.[46]

The insertion occurs over two stages, corresponding to the two parts of the excess chemical potential in Equation (15). The interaction of the inserted ion (i) with the other atoms (j) in the system is given by Equation (16).

$$U_{ij} = \lambda_A A e^{-Br_{ij}} - \lambda_C \frac{C}{r_{ij}^6} + \lambda_q \frac{q_i q_j}{4\pi\epsilon_0 r_{ij}} \quad (16)$$

First, the repulsive part of Buckingham interactions of the inserted ion are turned on by scaling the A parameter exponentially in 11 steps as:

$$\lambda_A = \frac{e^{10\lambda} - 1}{e^{10} - 1} \quad (17)$$

where λ is tuned linearly from 0 to 1 in 11 steps: λ = {0,0.1, …,0.9,1}. This scaling ensures that the inserted ion has a soft core and no discontinuities occur. The attractive part of the Buckingham interactions are then added by scaling the C parameter linearly in six steps by λ_C, where λ_C = {0,0.2, …,0.8,1}. Together, the free energy change of the system over these 16 steps sums up to μ_{vdW}^{EX}. Subsequently, the Coulomb interactions are added in 21 steps, with the charge on the inserted ion scaled by λ_q = {0,0.11,0.22, …, 0.55,0.6,0.65,0.7,0.725,0.75, …, 1}. The free energy change from adding the Coulomb interactions sums up to μ_{Coul}^{EX}. The number of steps for each part of the insertion is chosen to ensure that each ensemble overlaps sufficiently with its neighbors, while also limiting the computational cost.

Note that in these systems we calculate the chemical potential of single ions by inserting non-neutral species. The use of Ewald summations introduces a uniform background charge that keeps the simulation box neutral, but the insertion procedure neglects the free energy change of the charge crossing the interface between the gas and liquid phases.[47] However, the effect of system size will be minimal because of the high dielectric constant[48,49] and this surface term will cancel out in our calculations when we subtract the chemical potential of the carbonate and hydroxide ions in Equation (10). We have confirmed that inserting a neutral ion-pair (LiOH) and a triplet (Li_2CO_3) leads to an equivalent difference between the hydroxide and carbonate chemical potentials.

2.4 | Calculation of dissolved H_2O and CO_2 concentrations

To test the assumption that a negligible amount of gas is dissolved in the electrolyte, the concentrations of molecular H_2O (x_{H_2O}) and CO_2 (x_{CO_2}) in the melt were estimated. Although N_2 and O_2 are also present in flue gases, because these molecules have no polar bonds it is expected that their equilibrium concentration will be well below that of CO_2. For calculating x_{H_2O} and x_{CO_2}, we again assume that the dissolved gases are at a low concentration in the melt. Therefore, their presence does not affect the volume or the chemical potential of the molten carbonate and hydroxide. This assumption also implies that the excess chemical potential of H_2O and CO_2 is not a function of their concentrations and is equal to the solvation free energy (ΔG_X^{sol}). ΔG_X^{sol} can be computed as the free energy change from inserting one molecule into the molten salt phase.

Under these assumptions, the concentration of the dilute species follows Henry's law. Equating the chemical potential of the ideal gas and liquid of some species X gives

$$RT\ln\left(\frac{P_X}{P_0}\right) = RT\ln\left(\frac{N_X kT}{P_0\langle V\rangle}\right) + \Delta G_X^{sol} \quad (18)$$

where $\Delta_f G_X^0$ cancels. Assuming the species is dilute, the concentration can be converted to mole fraction (x_X) using

$$\frac{N_X}{\langle V\rangle} = \frac{x_X N}{\langle V\rangle} \approx \frac{x_X N_{salt}}{\langle V\rangle_{salt}} \quad (19)$$

where N is the total number of molecules, $\langle V\rangle$ is the total simulation volume, N_{salt} is the number of carbonate and hydroxide molecules, and $\langle V\rangle_{salt}$ is the volume of the carbonate and hydroxide molecules without any dilute species present. Combining Equations (18) and (19) yields a linear relationship between x_X and P_X:

$$x_X = \frac{P_X v_{salt}}{RT} \exp\left(-\frac{\Delta G_X^{sol}}{RT}\right) \quad (20)$$

where v_{salt} is the molar volume of the pure molten electrolyte.

2.5 | Molecular dynamics simulations

All calculations were performed in the NPT ensemble using the GROMACS simulation package, v.2018.[50,51] A cutoff of 1.0 nm was used for the non-bonded interactions, and the long-range electrostatic interactions were treated by using a smooth-particle-mesh Ewald technique. For the Buckingham interactions, long-range corrections to energy and pressure were applied. The equations of motion were integrated with a time-step of 1 ps. For computing μ_{vdW}^{EX}, we employed an efficient leap-frog stochastic dynamics (SD) integrator to integrate the equations of motion. This ensures a better sampling of the states at which the inserted ion is weakly interacting with the rest of the system. On the other hand, to calculate μ_{Coul}^{EX}, the equations of motion were integrated using the leap-frog (MD) algorithm, and the temperature was controlled using the canonical velocity-rescale thermostat.[52] This velocity-rescale thermostat correctly samples the canonical ensemble and frequently experiences fewer issues with equilibration of internal degrees of freedom than the Nosé–Hoover approach,[53,54] as discussed in Reference 52. The Parrinello–Rahman barostat[55] was applied to control the pressure in all simulations. The O—H covalent bond was constrained via the LINCS constraint-algorithm.

The excess chemical potential simulations were performed with five alkali cation mixtures to investigate the effect of cation composition on the chemical reaction equilibrium. The cation compositions studied are: $Li_{0.4}K_{0.6}$, $Li_{0.5}K_{0.5}$, $Li_{0.6}K_{0.4}$, $Li_{0.5}Na_{0.5}$, and $Na_{0.5}K_{0.5}$. The total number of cations was always held fixed at 1,000, whereas the carbonate/hydroxide ratio was varied to obtain carbonate mole fractions between 0 and 1. We have chosen more state points with a

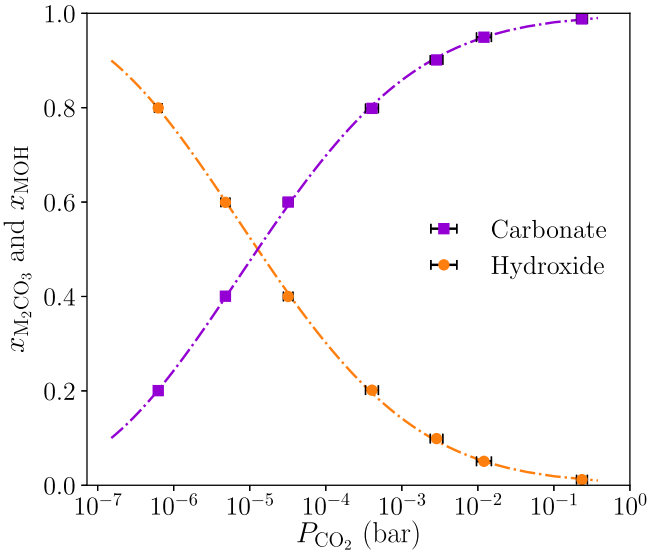

FIGURE 2 Chemical reaction equilibrium for a cation composition of 40% Li^+ and 60% K^+ at 923.15 K and a total pressure of 1 bar. P_{H_2O} is constant at 0.1 bar. The lines show fits of the three component Wilson equation[60] to the simulation results. The *y*-axis displays the mole fractions of the neutral salts where M represents a cation. The error bars show one standard error in the mean and are not displayed when smaller than the point [Color figure can be viewed at wileyonlinelibrary.com]

higher fraction of carbonate than hydroxide because these compositions more closely resemble those observed in realistic molten carbonate fuel cells. Details of the simulated systems are summarized in Table S5–S9. All systems were simulated in their liquid state at 923.15 K except for the $Na_{0.5}K_{0.5}$ mixture, which was studied at 1,023.15 K due to its higher melting point (~992 K).[56]

The calculation of dissolved CO_2 and H_2O was performed for a cation composition of $Li_{0.6}K_{0.4}$ at 923.15 K. The systems again consisted of 1,000 cations with a varied concentration of hydroxide and carbonate.

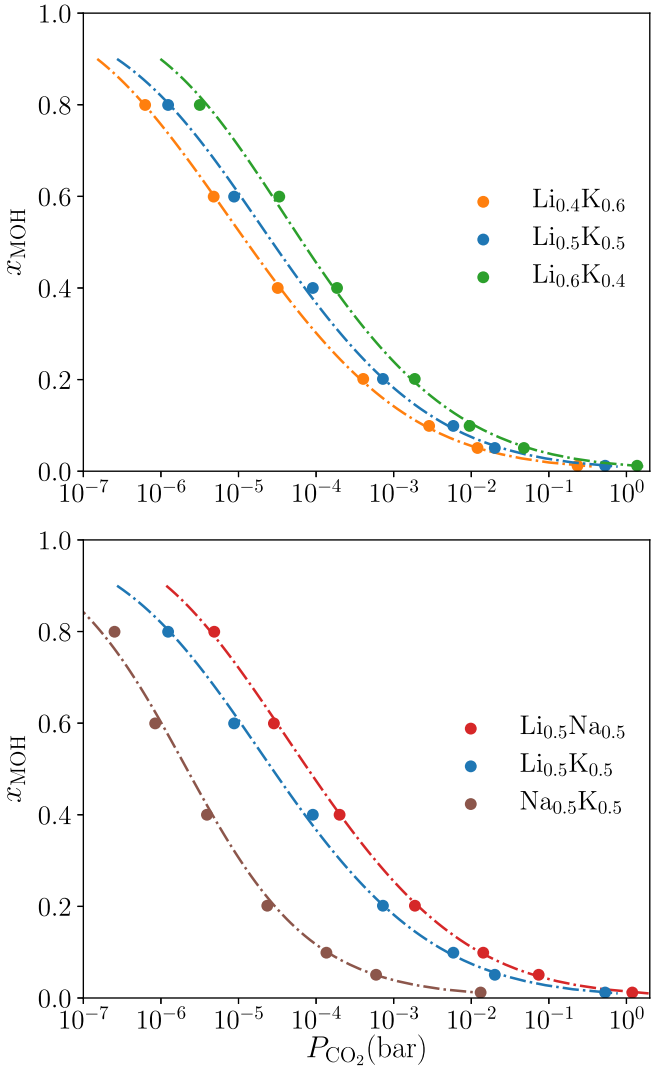

FIGURE 3 Equilibrium concentration of hydroxide for different cation compositions. All results are at 923.15 K and a total pressure of 1 bar, except for that of $Na_{0.5}K_{0.5}$ which is at 1023.15 K. P_{H_2O} is constant at 0.1 bar. The lines show fits of the three-component Wilson equation[60] to the simulation results. The *y*-axis displays the mole fraction of the neutral hydroxide salt where M represents a cation [Color figure can be viewed at wileyonlinelibrary.com]

3 | RESULTS AND DISCUSSION

Figure 2 gives the dependence of the equilibrium composition of the molten $Li_{0.4}K_{0.6}$ electrolyte as a function of the partial pressure of CO_2. In these calculations, P_{H_2O} is fixed at 0.1 bar, with other inert components in the gas-phase adding up to a total system pressure of 1 bar. As expected, when P_{CO_2} is near 1 bar, the molten electrolyte is mostly composed of carbonates, but as P_{CO_2} decreases, the concentration of hydroxide in the melt begins to increase. The error bars in this figure are of a similar size as the points and show the uncertainty in the equilibrium P_{CO_2} estimated from five independent simulations of the chemical potential in the melt. Because of the computational expense of these calculations, uncertainty is only calculated for this cation composition. The uncertainty for the other equilibrium curves shown in Figure 3 should be comparable to that of Figure 2, although greater by $\sqrt{5}$ times because only one simulation is performed at each composition.

Figure 3 presents the chemical reaction equilibria for five different cation compositions as a function of P_{CO_2} with P_{H_2O} constant at 0.1 bar. Corresponding values of the chemical potential of CO_3^{2-} and OH^- as a function of hydroxide concentration are provided in Tables S5–S9. Our results indicate that increasing lithium concentration increases the amount of hydroxide in the melt, while changing the cations from Li^+ to Na^+ to K^+ reduces the hydroxide fraction. This observation can be justified in terms of the "Hard-Soft Acid–Base" (HSAB) theory[57-59] which explains that soft acids or bases tend to be large and polarizable, while hard acids or bases are small and non-polarizable. The theory states that hard acids prefer to bond with hard

bases, and correspondingly soft acids prefer to bond with soft bases. In HSAB theory, OH^- is a hard anion while CO_3^{2-} is a softer anion. Thus, hydroxide is more stable in the presence of the harder, smaller cations, such as Li^+. Melts with more lithium have the highest hydroxide concentration, while melts with more potassium have the highest carbonate concentration.

The simulation results in Figures 2 and 3 are fit with a three-component Wilson activity coefficient model.[60] The fit parameters and the reference state chemical potentials are given in Tables S10 and S11. This model is able to accurately capture the single ion activity coefficient behavior. Because activity coefficients at any concentration can be calculated from this correlation, it is possible to find the reaction equilibrium at different gas phase compositions and extrapolate outside the range of the simulation data.

The experimental ionic conductivities of the investigated alkali carbonate mixtures are provided in Table 1.[61] The conductivity is highest for the $Li_{0.5}Na_{0.5}$ mixture and decreases with increasing concentrations of larger cations, matching the trend in hydroxide fraction. From the perspective of ionic conductivity, more lithium and sodium will improve the fuel cell performance. However, higher Li^+ concentrations also lead to more hydroxide in the melt. Therefore, there is a trade-off between conductivity and CO_2 separation efficiency, meaning that an optimum cation mixture must be determined for each exact situation.

The assumption that the dissolved concentrations of CO_2 and H_2O in the melt are low and will have a negligible effect on the calculations is tested by calculating their Henry's law constants in the $Li_{0.6}K_{0.4}$ carbonate-hydroxide melt. These constants are computed as a function of hydroxide mole fraction and the results are tabulated in Table 2. At a given partial pressure the Henry's law constants can be used to estimate the solubility of a species in a liquid since these two quantities are directly proportional.

Using the Henry's law constants, the concentrations of dissolved CO_2 and H_2O are plotted in Figure 4 as a function of CO_2 partial pressure, with the partial pressure of water held fixed at 0.1 bar. We found that the concentration of water is over two orders of magnitude higher than that of CO_2 for all partial pressures investigated. Because water is a polar molecule and has the propensity to form hydrogen bonds, it is more stable in the melt of ions. As the partial pressure of CO_2 decreases, the amount of CO_2 dissolved decreases, as would be expected. However, the amount of dissolved H_2O increases, due to the increasing fraction of hydroxide in the melt, as shown in Figure 3.

At the lowest P_{CO_2} (highest OH^- concentration) studied, water is predicted to make up approximately 2 mol% of the melt, if equilibrium is achieved. This fraction is high enough to break some of the assumptions made in the calculation of the dissolved water concentration as well as the carbonate-hydroxide chemical equilibrium. However, these majority hydroxide states are unlikely to be present in practical MCFCs, and the partial breaking of the assumptions does not affect our main conclusions.

As evident from Table 2 of the SI and Figure 4, CO_2 exhibits a poor solubility in this melt irrespective of the hydroxide mole fraction. Although there is a low solubility of molecular CO_2, the dissolved CO_2 can react with the carbonate ions to form pyrocarbonate ($C_2O_5^{2-}$).[37] Based on the ab initio molecular dynamics study by Corradini et al,[37] the amount of dissolved pyrocarbonate ($C_2O_5^{2-}$) is expected to be significant in these electrolytes compared to the fraction of dissolved CO_2. The pyrocarbonate concentration can be estimated by following a similar approach to that used in this work to determine the dissolved

TABLE 1 Experimental ionic conductivity, σ, of molten alkali carbonate mixtures at 1,050 K[61]

System	σ (S/m)
$Li_{0.5}Na_{0.5}$	295
$Li_{0.6}K_{0.4}$	218
$Li_{0.5}K_{0.5}$	188
$Li_{0.4}K_{0.6}$	183
$Na_{0.5}K_{0.5}$	188

TABLE 2 Henry's law constant (k_H, bar^{-1}) of CO_2 and H_2O in $Li_{0.6}K_{0.4}$ carbonate-hydroxide mixture at 923.15 K and a total pressure of 1 bar

x_{OH}^-	$k_H(CO_2)$	$k_H(H_2O)$
0.80	5.73×10^{-7}	2.04×10^{-1}
0.60	3.11×10^{-7}	5.41×10^{-2}
0.40	1.61×10^{-7}	1.64×10^{-2}
0.20	1.01×10^{-7}	3.98×10^{-3}
0.10	7.89×10^{-8}	1.38×10^{-3}
0.05	6.31×10^{-8}	6.65×10^{-4}
0.01	7.12×10^{-8}	3.19×10^{-4}

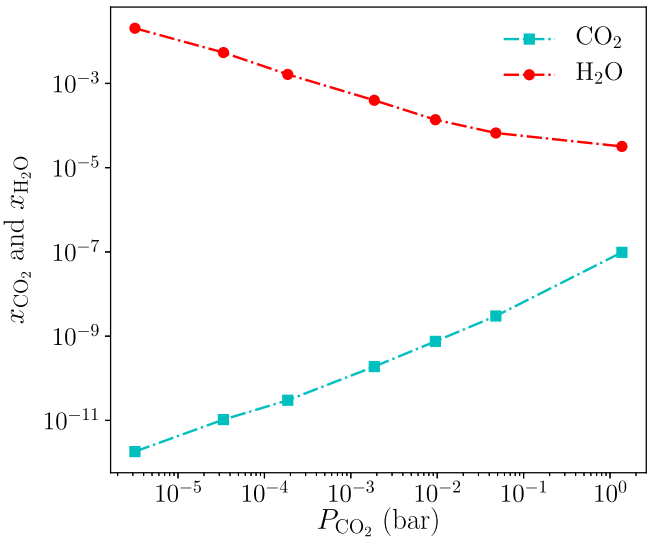

FIGURE 4 Concentration of CO_2 and H_2O dissolved in carbonate-hydroxide melt with a cation composition of 60% Li^+ and 40% K^+ at 923.15 K and a total pressure of 1 bar. P_{H_2O} is constant at 0.1 bar [Color figure can be viewed at wileyonlinelibrary.com]

concentrations of CO_2 and H_2O, and is a future objective of our research.

4 | CONCLUSIONS

Our simulations of molten alkali carbonates/hydroxides in equilibrium with gas phases containing water and carbon dioxide show that a significant amount of hydroxide can be present in the electrolyte when the partial pressure of CO_2 is low compared to that of H_2O. We also find that the concentration of dissolved water in the melt is higher than that of solvated CO_2, although these calculation do not take into consideration potential reactive stabilization of H_2O and CO_2 with the anions. At low partial pressures of CO_2, the concentration of hydroxide in the melt can be high enough that it may significantly contribute to oxygen and electron transfer within MCFCs. This could account for some of the non-carbonate current observed in MCFCs at low cathode CO_2 concentration.[13]

The equilibrium hydroxide concentration in the melt also depends on the cation composition, with smaller (harder) cations leading to more hydroxide in the molten carbonate phase. Therefore, a balance must be struck between the higher ionic conductivity from smaller cations and the decrease in CO_2 separation due to hydroxide formation.

There are a number of outstanding questions about the MCFC electrolyte that warrant further work. The effect of hydroxide on properties such as the conductivity, viscosity, and transport mechanism is important to understand to improve MCFC electrical efficiency and effectiveness at capturing CO_2. Classical force fields are not able to capture the role of ongoing reactions; however, such effects can be investigated within an ab initio molecular dynamics framework. In addition, even though the concentrations of dissolved molecular CO_2 and H_2O are small, these gases can react with the molten carbonate and hydroxide to form more charged species such as pyrocarbonate and bicarbonate. Furthermore, the oxygen present in the system may form oxide and other charged oxygen species.[38,39] To determine the concentrations of these species, models compatible with those used here for carbonate and hydroxide need to be developed. These and similar topics will be addressed in future work.

ACKNOWLEDGMENTS

Financial support for this work was provided by ExxonMobil, under agreement EM09125.A1, and by the Office of Basic Energy Sciences, U.S. Department of Energy, under Award DE-SC0002128. Computing resources were provided by Princeton Research Computing.

CONFLICT OF INTEREST

The Princeton authors declare no potential conflict of interest. Timothy A. Barckholtz, Gabor Kiss, and Lucas Koziol are all employees of ExxonMobil, which is currently working on commercializing this technology in the industrial and power sectors.

AUTHOR CONTRIBUTIONS

Jeffrey M. Young and Anirban Mondal have contributed equally to this work by designing research, executing the simulations, analyzing data, and writing the manuscript. Other authors contributed by designing research and analyzing the data, and edited the manuscript.

ORCID

Jeffrey M. Young https://orcid.org/0000-0001-8879-5132
Anirban Mondal https://orcid.org/0000-0003-3029-8840
Athanassios Z. Panagiotopoulos https://orcid.org/0000-0002-8152-6615

REFERENCES

1. Tomczyk P. MCFC versus other fuel cells-characteristics, technologies and prospects. *J Power Sources*. 2006;160:858-862.
2. Caprile L, Passalacqua B, Torazza A. Carbon capture: energy wasting technologies or the MCFCs challenge? *Int J Hydrogen Energy*. 2009; 36:10269-10277.
3. Wee JH. Carbon dioxide emission reduction using molten carbonate fuel cell systems. *Renew Sustain Energy Rev*. 2014;32:178-191.
4. Molenda J, Kupecki J, Baron R, et al. Status report on high temperature fuel cells in Poland - recent advances and achievements. *Int J Hydrogen Energy*. 2017;42:4366-4403.
5. Cassir M, McPhail SJ, Moreno A. Strategies and new developments in the field of molten carbonates and high-temperature fuel cells in the carbon cycle. *Int J Hydrogen Energy*. 2012;37:19345-19350.
6. Heydorn EC. *Validation of an Integrated Hydrogen Energy Station*. Washington D.C.: Air Products and Chemicals, Inc; 2012.
7. Gharieh K, Jafari MA, Guo Q. Investment in hydrogen tri-generation for wastewater treatment plants under uncertainties. *J Power Sources*. 2015;297:302-314.
8. Kim YS, Lim JH, Chun HS. Creep mechanism of porous MCFC Ni anodes strengthened by Ni_3Al. *AIChE J*. 2006;52(1):359-365.
9. Antolini E. The stability of molten carbonate fuel cell electrodes: a review of recent improvements. *Appl Energy*. 2011;88(12):4274-4293.
10. Nguyen HVP, Othman MR, Seo D, et al. Nano Ni layered anode for enhanced MCFC performance at reduced operating temperature. *Int J Hydrogen Energy*. 2014;39(23):12285-12290.
11. Morita H, Mugikura Y, Izaki Y, Watanabe T, Abe T. Model of cathode reaction resistance in molten carbonate fuel cells. *J Electrochem Soc*. 1998;145(5):1511-1517.
12. Morita H, Komoda M, Mugikura Y, et al. Performance analysis of molten carbonate fuel cell using a Li/Na electrolyte. *J Power Sources*. 2002;112:509-518.
13. Rosen J, Geary T, Hilmi A, et al. Molten carbonate fuel cell performance for CO_2 capture from natural gas combined cycle flue gas. *J Electrochem Soc*. 2020;167:064505.
14. Nishina T, Ohuchi S, Yamada K, Uchida I. Water effect on oxygen reduction in molten $(Li + K)CO_3$ eutectic. *J Electroanal Chem*. 1996; 408:181-187.
15. Evans A, Xing W, Norby T. Electromotive force (EMF) determination of transport numbers for native and foreign ions in molten alkali metal carbonates. *J Electrochem Soc*. 2015;162(10):1135-1143.
16. Mohn H, Wendt H. Molecular thermodynamics of molten salt evaporation IV. The evaporation of molten carbonates in atmospheres containing CO_2 and water vapour. *Z Phys Chem*. 1995;192: 101-119.
17. Pomfret MB, Owrutsky JC, Walker RA. High-temperature Raman spectroscopy of solid oxide fuel cell materials and processes. *J Phys Chem B*. 2006;110(35):17305-17308.

18. Turner CH, Brennan JK, Lisal M, Smith WR, Karl Johnson J, Gubbins KE. Simulation of chemical reaction equilibria by the reaction ensemble Monte Carlo method: a review. *Mol Simul*. 2008;34(2):119-146.
19. Meuwly M. Reactive molecular dynamics: from small molecules to proteins. *Wiley Interdiscip Rev: Comput Mol Sci*. 2019;9(1):1-22.
20. Smith WR, Qi W. Molecular simulation of chemical reaction equilibrium by computationally efficient free energy minimization. *ACS Cent Sci*. 2018;4:1185-1193.
21. Behler J. First principles neural network potentials for reactive simulations of large molecular and condensed systems. *Angew Chem*. 2017; 56(42):12828-12840.
22. Tissen JTWM, Janssen GJM. Molecular-dynamics simulation of molten alkali carbonates. *Mol Phys*. 1990;71(2):413-426.
23. Habasaki J. Molecular dynamics simulation of molten Li_2CO_3 and Na_2CO_3. *Mol Phys*. 1990;69(1):115-128.
24. Costa MF. Molecular dynamics of molten Li_2CO_3-K_2CO_3. *J Mol Liq*. 2008;138(1):61-68.
25. Corradini D, Coudert FX, Vuilleumier R. Insight into the Li_2CO_3-K_2CO_3 eutectic mixture from classical molecular dynamics: thermodynamics, structure, and dynamics. *J Chem Phys*. 2016;144(10):104507.
26. Desmaele E, Sator N, Vuilleumier R, Guillot B. Atomistic simulations of molten carbonates: thermodynamic and transport properties of the Li_2CO_3-Na_2CO_3-K_2CO_3 system. *J Chem Phys*. 2019;150(9):094504.
27. Okazaki S, Ohtori N, Okada I. Molecular dynamics studies on molten alkali hydroxides. I. Static properties of molten LiOH. *J Chem Phys*. 1990;92(12):7505-7514.
28. Mondal A, Young JM, Barckholtz TA, Kiss G, Koziol L, Panagiotopoulos AZ. Genetic Algorithm Driven Force Field Parameterization for Molten Alkali-Metal Carbonate and Hydroxide Salts J Chem Theory Comp; 2020; https://doi.org/10.1021/acs.jctc.0c00285.
29. Mason EA, Rice WE. The intermolecular potentials of helium and hydrogen. *J Chem Phys*. 1954;22(3):522-535.
30. Mirskaya KV. Combining rules for interatomic potential functions of Buckingham form. *Tetrahedron*. 1973;29(5):679-682.
31. Tsuzuki S, Uchimaru T, Mikami M, Tanabe K, Sako T, Kuwajima S. Molecular dynamics simulation of supercritical carbon dioxide fluid with the model potential from Ab initio molecular orbital calculations. *Chem Phys Lett*. 1996;255(4–6):347-349.
32. Cygan RT, Romanov VN, Myshakin EM. Molecular simulation of carbon dioxide capture by Montmorillonite using an accurate and flexible force field. *J Phys Chem C*. 2012;116(24):13079-13091.
33. Wade AD, Wang LP, Huggins DJ. Assimilating radial distribution functions to build water models with improved structural properties. *J Chem Inf Model*. 2018;58(9):1766-1778.
34. Chase MW. *NIST-JANAF Thermochemical Tables*. 4th ed. Washington, DC: American Chemical Society; 1998.
35. Claes P, Moyaux D, Solubility PD. Solvation of carbon dioxide in the molten Li_2CO_3/Na_2CO_3/K_2CO_3 (43.5:31.5:25.0 Mol%) eutectic mixture at 973 K. part I. experimental part. *Eur J Inorg Chem*. 1999;1999 (4):583-588.
36. Zhang L, Huang X, Qin C, et al. First spectroscopic identification of Pyrocarbonate for high CO_2 flux membranes containing highly interconnected three dimensional ionic channels. *Phys Chem Chem Phys*. 2013;15:13147-13152.
37. Corradini D, Coudert FX, Vuilleumier R. Carbon dioxide transport in molten calcium carbonate occurs through an Oxo-Grotthuss mechanism via a pyrocarbonate anion. *Nat Chem*. 2016;8(5):454-460.
38. Appleby AJ, Nicholson SB. Reduction of oxygen in alkali carbonate melts. *J Electroanal Chem*. 1977;83(2):309-328.
39. Chen LJ, Cheng X, Lin CJ, Huang CM. In-situ Raman spectroscopic studies on the oxide species in molten Li/K_2CO_3. *Electrochim Acta*. 2002;47(9):1475-1480.
40. Li XW, Shibata E, Nakamura T. Theoretical calculation of thermodynamic properties of polybrominated Dibenzo-p-dioxins. *J Chem Eng Data*. 2003;48(3):727-735.
41. Zeng Q, Su K, Zhang L, Xu Y, Cheng L, Yan X. Evaluation of the thermodynamic data of CH_3SiCl_3 based on quantum chemistry calculations. *J Phys Chem Ref Data Monogr*. 2006;35(3):1385-1390.
42. Awasthi N, Ritschel T, Lipowsky R, Knecht V. Standard Gibbs energies of formation and equilibrium constants from *Ab Initio* calculations: covalent dimerization of NO_2 and synthesis of NH_3. *J Chem Thermodyn*. 2013;62:211-221.
43. Allison TC, Burgess DR. First-principles prediction of enthalpies of formation for polycyclic aromatic hydrocarbons and derivatives. *J Phys Chem A*. 2015;119(46):11329-11365.
44. Frisch MJ, Trucks GW, Schlegel HB, Scuseria GE, Robb MA, Cheeseman JR, Scalmani G, Barone V, Petersson GA, Nakatsuji H, Li X, Caricato M, Marenich AV, Bloino J, Janesko BG, Gomperts R, Mennucci B, Hratchian HP, Ortiz JV, Izmaylov AF, Sonnenberg JL, Williams-Young D, Ding F, Lipparini F, Egidi F, Goings J, Peng B, Petrone A, Henderson T, Ranasinghe D, Zakrzewski VG, Gao J, Rega N, Zheng G, Liang W, Hada M, Ehara M, Toyota K, Fukuda R, Hasegawa J, Ishida M, Nakajima T, Honda Y, Kitao O, Nakai H, Vreven T, Throssell K, Montgomery Jr JA, Peralta JE, Ogliaro F, Bearpark MJ, Heyd JJ, Brothers EN, Kudin KN, Staroverov VN, Keith TA, Kobayashi R, Normand J, Raghavachari K, Rendell AP, Burant JC, Iyengar SS, Tomasi J, Cossi M, Millam JM, Klene M, Adamo C, Cammi R, Ochterski JW, Martin RL, Morokuma K, Farkas O, Foresman JB, Fox DJ. Gaussian16 Revision C01; 2016.
45. Curtiss LA, Raghavachari K, Redfern PC, Pople JA. Assessment of Gaussian-2 and density functional theories for the computation of enthalpies of formation. *J Chem Phys*. 1997;106(3):1063-1079.
46. Bennett CH. Efficient estimation of free energy differences from Monte Carlo data. *J Comput Phys*. 1976;22(2):245-268.
47. Reif MM, Hünenberger PH. Origin of asymmetric solvation effects for ions in water and organic solvents investigated using molecular dynamics simulations: the swain acity-basity scale revisited. *J Phys Chem B*. 2016;120(33):8485-8517.
48. Hummer G, Pratt LR, García AE. Molecular theories and simulation of ions and polar molecules in water. *J Phys Chem A*. 1998;102(41): 7885-7895.
49. Hub JS, de Groot BL, Grubmüller H, Groenhof G. Quantifying artifacts in Ewald simulations of inhomogeneous systems with a net charge. *J Chem Theory Comput*. 2014;10(1):381-390.
50. Hess B, Kutzner C, Van Der Spoel D, Lindahl E. GROMACS 4: algorithms for highly efficient, load-balanced, and scalable molecular simulation. *J Chem Theory Comput*. 2008;4(3):435-447.
51. Pronk S, Páll S, Schulz R, et al. GROMACS 4.5: a high-throughput and highly parallel open source molecular simulation toolkit. *Bioinformatics*. 2013;29(7):845-854.
52. Bussi G, Donadio D, Parrinello M. Canonical sampling through velocity rescaling. *J Chem Phys*. 2007;126(1):014101.
53. Nosé S. A unified formulation of the constant temperature molecular dynamics methods. *J Chem Phys*. 1984;81(1):511-519.
54. Hoover WG. Canonical dynamics: equilibrium phase-space distributions. *Phys Rev A*. 1985;31:1695-1697.
55. Parrinello M, Rahman A. Polymorphic transitions in single crystals: a new molecular dynamics method. *J Appl Phys*. 1981;52(12):7182-7190.
56. Reisman A. Heterogeneous equilibria in the system K_2CO_3-Na_2CO_3. *J Am Chem Soc*. 1959;81(4):807-811.
57. Pearson RG. Hard and soft acids and bases. *J Am Chem Soc*. 1963;85 (22):3533-3539.
58. Pearson RG. Hard and soft acids and bases, HSAB, part I: fundamental principles. *J Chem Educ*. 1968;45(9):581.
59. Pearson RG. Hard and soft acids and bases, HSAB, part II: underlying theories. *J Chem Educ*. 1968;45(10):643-648.
60. Wilson GM. Vapor-liquid equilibrium. XI. A new expression for the excess free energy of mixing. *J Am Chem Soc*. 1964;86(2):127-130.
61. Janz GJ. Thermodynamic and transport properties for molten salts: correlation equations for critically evaluated density, surface tension,

electrical conductance, and viscosity data. *J Phys Chem Ref Data Monogr*. 1988;17(Suppl. 2):159-266.

SUPPORTING INFORMATION

Additional supporting information may be found online in the Supporting Information section at the end of this article.

How to cite this article: Young JM, Mondal A, Barckholtz TA, Kiss G, Koziol L, Panagiotopoulos AZ. Predicting chemical reaction equilibria in molten carbonate fuel cells via molecular simulations. *AIChE J*. 2021;67:e16988. https://doi.org/10.1002/aic.16988